Spatially Resolved Ions Imaging at Room Temperature

V. Kumar, N. Lausti, and M. Hejduk
Charles University, Faculty of Mathematics and Physics, Prague, Czech Republic.

Abstract. We present a simple and cost-effective imaging system consisting of relay lenses and an electron-multiplying CCD camera to efficiently detect ^{40}Ca atoms fluorescence during loading and $^{40}Ca^{+}$ ions during Doppler cooling. The setup provides a theoretical resolution at the micron level for both ^{40}Ca and $^{40}Ca^{+}$, with a magnification greater than 10x. For optimization of the signal acquired by the camera, we identify various noise sources and present the optimal setting of operation parameters that suppress them.

Introduction

Optical imaging systems are widely utilized in the physical and life sciences due to their capability to non-invasively capture details at microscopic and nanoscopic scales [*Wong-Campos et al.,* 2016]. Imaging of emitters, such as optical defects in solids [*Eva*, 2009], trapped atoms [*Blatt et al.*, 2012], and ions [*Leibfried et al.*, 2001], relies on the 'optical setup part' for efficient fluorescence collection and the 'detection systems' to capture light and produce high-quality images. Imaging systems for trapped ions are essential in various fields, including quantum computing, spectroscopy, and fundamental physics experiments, which enable to capture of detailed information about the ion's position, state, and interactions with their environment.

The principles involved, in general, while designing the optical setup for imaging systems of trapped ions are as follows.

- Maximizing light collection. This involves optimizing the numerical aperture (NA) of the lenses and minimizing optical losses through careful selection of mirrors and filters.
- Minimizing optical aberrations. High-quality optical components are used to minimize aberrations such as spherical aberration, chromatic aberration, and astigmatism, which can degrade image quality.
- Improving signal-to-noise ratio (SNR). Using high-efficiency detectors improves SNR by reducing background noise and enhancing the detection of weak signals from ions. Charged-coupled devices (CCDs) or electron-multiplying CCDs (EMCCDs) are often used to detect photons, which convert light into electronic signals and are then processed to form an image.

In addition, alignment and mechanical stability of the setup are also critical to prevent drift and maintain consistent imaging conditions. Therefore, the solid angle of the light collection with aberrations issues, setup stabilization, and camera sensor altogether is crucial to influencing the number of detected photons.

Here, we are reporting our imaging setup developed for ion trapping experiments, that is for imaging ^{40}Ca atoms fluorescence during loading and $^{40}Ca^{+}$ ions during Doppler cooling. Our optical setup is simple and cost-effective consisting of relay lenses and a couple of mirrors, which see the source through a top viewport of the vacuum chamber. For our detection purposes, we are using an EMCCD (Andor iXon U897) that offers many advantages for low-light applications. Photon counting capabilities, sub-electron readout noise, and low dark current make EMCCD ideal for low-light detection tasks [*Daigle et al.*, 2019].

The structure of this paper is as follows. Beginning with an introduction in Sect 1, we are reporting our optical setup development in Sect 2. We reviewed, discussed, and derived imaging mode and optimization from the detection system point of view in Sect 3 and finally concluded in Sect 4.

Imaging System

Developing an effective imaging setup for capturing photons emitted by trapped ions is crucial. Typically, in the case of a single species, a multi-lens system positioned outside the vacuum chamber is the conventional approach [*Alt,* 2002*; Noek et al.*, 2013; *Wong et al.*, 2016; *Nordmann et al.*, 2023]. We have followed a similar approach in designing our setup as well. Our imaging setup illustrated in Fig 1 is configured with all optical components positioned outside the chamber, maintaining a working distance of 17 mm from the top viewport glass, which has a thickness of 6.0 mm and a diameter of 90.0 mm. Additionally, the distance from the vacuum chamber center (or trap center) to the viewport is 78.5 mm.

The fluorescence emitted by the species through the top viewport is initially gathered by a wide objective planoconvex lens (L_1). Subsequently, the collected light is collimated towards a second fixed planoconvex lens (L_2). The focused light is then further recollimated by a third small planoconvex lens (L_3). Using the two highly reflecting mirrors ($M_1, M_2 > 99.9\%$), the fluorescent photons can be directed toward the camera sensor, facilitated by a fourth biconvex lens (L_4). Each L_1, L_3 and L_4 are moveable along its principal axis. To mitigate

the presence of stray light, the entire pathway is enclosed within a cage system. Additionally, to selectively capture the specific wavelengths, narrow band-pass filters is an option before the camera sensor, which can facilitate the detection of ^{40}Ca atoms fluorescence during loading and of $^{40}Ca^{+}$ ions during Doppler cooling.

To characterize the proficiency of the imaging setup, the numerical aperture $NA(\vartheta, \eta) = n.\sin\vartheta$, measuring the angular acceptance of incoming light, is a key. Here n is the refractive index and ϑ is the half-angle of the maximum light cone entering the system. For a lens, ϑ can be approximated by $D/2f$, where D is the aperture diameter and f is the focal length. Our setup has a NA of 0.375, providing a resolution of 1.37 μm for ^{40}Ca and 1.29 μm for $^{40}Ca^{+}$.

Given the NA, the solid angle specifies the amount of light emitted by the ions that can be collected over a segment of a unit sphere $\Omega/4\pi = (1 - \sqrt{1 - NA^2})/2$ is $\Omega/4\pi \approx 3.65\%$ (or $\Omega \approx 0.46$ steradians). Let ξ be the fluorescent photon rate from a trapped ion in the vacuum chamber. Depending on the exposure time[1] t_e, the number of photons per ion per exposure is ξt_e, and approximately $\xi t_e \Omega/4\pi$ photons are collected by the camera sensor over the solid angle fraction of the imaging system. Considering the camera sensor's efficiency η, the photons read per exposure is $\xi t_e \eta \Omega/4\pi$. If an ion takes $n_1 \times n_2$ pixels on the camera, the photons detected per pixel per exposure per ion is given by Eq (1), where i, j is the camera pixel having coordinate (x_i, y_j).

$$\mathcal{U}(x_i, y_j) = \frac{\xi t_e \eta}{n_1 \times n_2}\left(\frac{1}{2} - \frac{1}{2}\sqrt{1 - NA^2}\right). \quad (1)$$

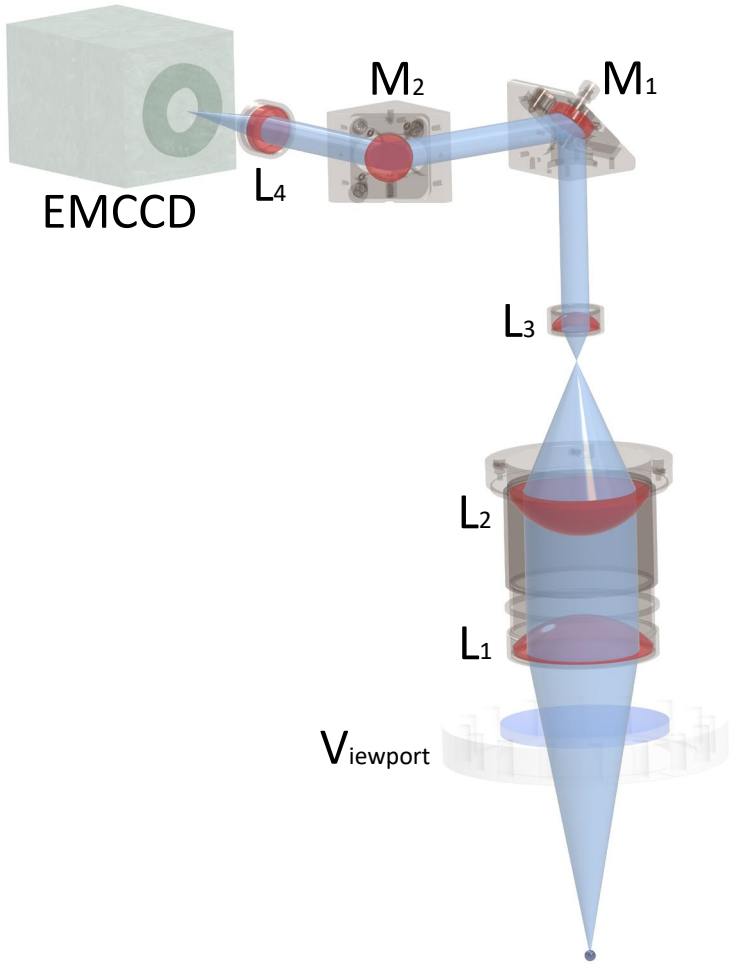

Figure 1. Illustration of the imaging setup consisting of relay lenses and EMCCD camera (not scaled). The total length of the imaging setup, extending from the objective lens to the camera sensor is 95 cm. Lenses are contained within a tube secured by threaded rings, and mirrors are mounted using right-angle kinematic mirror mounts within a cage system. The distances between optical elements (mentioned in Table 1) are as follows: $L_1L_2 = 60 \pm x_1$ mm, $L_2L_3 = 115 \pm x_2$ mm, $L_3M_1 = 100 \pm x_3$ mm, $M_1M_2 = 100$ mm, $M_2L_4 = 100$ mm, and L_4 to the camera is 100 mm. x_j for $j \in [1, 3]$ are tunable.

[1]It is the interval during which camera collects light prior readout. In general, it is inversely proportional to the shutter speed.

In addition NA for the evaluation of $\mathcal{U}(x_i, y_j)$, magnification of the setup is also vital information, that determines the image's relative size concerning the object. For this purpose, the ABCD matrix is used, which depends on light propagation through an arbitrary optical system based on the paraxial approximation of optics in cascade. Eq (2) is the resultant ABCD matrix of our setup denoted by M_I, involving optics parameters and spacing.

$$M_I = \begin{bmatrix} y_1 + y_2\frac{1-n}{r_1} & y_1\frac{t_1}{n} + y_2\left(1 + \frac{t_1}{r_1}\frac{1-n}{n}\right) + d_1\left(y_1 + y_2\frac{1-n}{r_1}\right) \\ y_3 + y_4\frac{1-n}{r_1} & y_3\frac{t_1}{n} + y_4 y_4\left(1 + \frac{t_1}{r_1}\frac{1-n}{n}\right) + d_1\left(y_3 + y_4\frac{1-n}{r_1}\right) \end{bmatrix}. \quad (2)$$

The calculated spatial magnification is ≈ 11.4 for ^{40}Ca atoms and ≈ 11.6 for $^{40}Ca^{+}$ ions. The variables y_k for $k\epsilon[1,4]$ are detailed in the appendix A1. Appendix A2 describes imaging dynamics for both ^{40}Ca and $^{40}Ca^{+}$.

Imaging Mode and Optimisation

For the efficient spatial resolution of localized ions, it is well understood that the proper background noise analysis in addition to optimal optical setup is important. To meet objectives from the detection perspectives, pixel binning, timing protocols, etc play significant roles which are later discussed in this section.

Depending on mean photon flux in an exposure, i.e. $\mathcal{U}(x_i, y_j)$, the photoelectrons per pixel produced is $n_{ij} = \eta\mathcal{U}(x_i, y_j)$, where $\eta = \eta(\lambda, T)$ is the quantum efficiency of EMCCD that depends on wavelength λ of fluorescent photons and operating temperature T. At 25 °C, the efficiency function based on non-linear curve fitting in a range from 225 nm to 825 nm determined is $\eta(\lambda, T = 25\,°C) = 5575\lambda^5 + 676\lambda^4 + 23\lambda^3 + 676\lambda^2 + \lambda + 456$, which at 397 nm is 78%. The quantum efficiency (%) vs wavelength (nm) curve of our blue-optimized sensor for quantum and BEC studies was obtained from the 2022 specification sheet by Oxford Instruments. Table 2 describes the specifications of our camera, which has digitization of 16 bit at all speeds.

Table 1. Optics list of the imaging setup. Mirrors reflectance $> 99\%$ is for the wavelength range 395 nm to 975 nm for the angle of incidence of 8°. The refractive index of N-BK7 at 397 nm and 422 nm are 1.531 and 1.528 respectively[2].

Optics	**Description**	**Radius of curvature** (in mm)	**Focal length** (in mm)	**Thickness** (in mm)
Lens L_1	LA1238-A, N-BK7 Plano-convex, Ø75.0 mm, AR coated	$r_1 = 51.5$	$99.7 \pm 1\%$	$t_1 = 19.2$
Lens L_2	LA1740-A, N-BK7 Plano-convex, Ø75.0 mm, AR coated	$r_2 = 43.8$	$84.7 \pm 1\%$	$t_2 = 24.2$
Lens L_3	LA1805, N-BK7 Plano-convex, Ø25.4 mm, AR coated	$r_3 = 15.5$	$29.9 \pm 1\%$	$t_3 = 8.6$
Mirrors (M_1, M_2)	BB1-E02P, Broadband dielectric mirror, Ø25.4 mm, Back side polished			6
Lens L_4	LB1676-A, N-BK7 Bi-convex lens, Ø25.4 mm, AR coated	$r_4 = 102.4$	$99.7 \pm 1\%$	$t_4 = 3.6$

Table 2. Technical parameters of the camera with timestamp accuracy 10 ns. The electron multiplier (EM) gain in absolute linear is $1 - 1000$ at all cooling temperatures.

Pixels	**Pixel well depth** (PWD)	**Amplifier** (Read-out)						**Shift time** (in µs)
Active pixels ($H \times V \equiv 512 \times 512$)	Active area PWD 180 000 e$^-$	Conventional mode			EMCCD mode			Sensor row vertical shift (t_v)
Pixel size ($W \times H \equiv 16 \times 16$ µm)	Gain register PWD 800 000 e$^-$		Read noise (e$^-$), $S_{r,\mathrm{CCD}-h}$			Read noise (e$^-$), $S_{r,\mathrm{EMCCD}-h}$		0.3, 0.5, 0.9, 1.7, and 3.3 (user selectable)
Image area (with 100% fill factor) 8.2 × 8.2 mm^2		$f_{\mathrm{CCD}-h}$ (MHz)	EM (OFF)	EM (ON)	$f_{\mathrm{EMCCD}-h}$ (MHz)	EM (OFF)	EM (ON)	
		0.08	2.7	–	1	15	< 1	
		1	5.3	–	5	37	< 1	
		3	9.6	–	10	65	< 1	
					17	89	< 1	

[2](https://refractiveindex.info/?shelf=glass&book=BK7&page=SCHOTT).

Depending on the time, wavelength, several noises, etc, given that $\boldsymbol{S}_r\left(x_i, y_j; \lambda, t_e, T; S_c, S_r, F, g\right)$ is signal recorded by a camera, Eq (3) is a combination of the 'required signal $\boldsymbol{\mathcal{R}}\left(x_i, y_j; \lambda, t_e, T; F\right)$' and 'error signal $\boldsymbol{\mathcal{E}}(t_e, T; S_c, S_r, F, g)$'. Involved terms S_c and S_r are clock-induced charge[3] (CIC) noise and readout noise[4] (RN) respectively, while F is the noise factor[5] and g is the multiplication gain[6]. $g = 1$ means gain OFF and the camera works in conventional CCD mode otherwise $g > 1$ means camera works in EMCCD mode. $I_d(T)$ (in $e^-/px/s$) is the dark current as a function of temperature.

$$\boldsymbol{S}_r\left(x_i, y_j; \lambda, t_e, T; S_c, S_r, F, g\right) = \boldsymbol{S}(\boldsymbol{\mathcal{R}}, \boldsymbol{\mathcal{E}}) = \sqrt{\underbrace{F^2\eta(\lambda, T)\mathcal{U}\left(x_i, y_j\right)}_{=\boldsymbol{\mathcal{R}}^2\left(x_i, y_j; \lambda, t_e, T; F\right)} + \underbrace{F^2\{I_d(T)t_e + S_c\} + \frac{S_r^2}{g^2}}_{=\boldsymbol{\mathcal{E}}^2(t_e, T; S_c, S_r, F, g)}}. \tag{3}$$

$\boldsymbol{S}_r(\boldsymbol{\mathcal{R}}, \boldsymbol{\mathcal{E}})$ is the multivariate optimization problem with the objective of minimizing $\boldsymbol{\mathcal{E}}^2(t_e; S_c, S_r, F, g)$, express by

$$\text{min.}\left[\boldsymbol{S}_r\left(x_i, y_j; \lambda, t_e, T; S_c, S_r, F, g\right)\right] \rightarrow \text{min.}\left[\boldsymbol{\mathcal{E}}^2(t_e, T; S_c, S_r, F, g)\right] \geq 0\,. \tag{4}$$

The related constraints, in terms of involved variables, are the essential features of the problem mentioned in Eq (4). Typically, it is spatial independent, but in situations such as super-resolution microscopy of single atoms in optical lattices [*Alberti et al.,* 2016], the $\boldsymbol{S}_r(\boldsymbol{\mathcal{R}}, \boldsymbol{\mathcal{E}})$ optimization is spatial dependent. That involves $S_s = S_s\left(x_i, y_j\right)$ and S_p as additional terms. $S_s\left(x_i, y_j\right)$ is the stray light shot noise, while S_p is the photo response non-uniformity noise. Here, we will stick with Eq (4) spatial independent scenario only.

This optimization problem can be realized geometrically in Fig 2 and can be named as imaging Pythagorean pentagonal. Depending on the main right-angled triangle OO_1O_2 of imaging pentagonal $OO_1O_2O_3O_4$ contributed by traingles OO_2O_3 and OO_3O_4, the signal to noise ratio of the system, let denote by $SNR(\boldsymbol{\mathcal{R}}, \boldsymbol{\mathcal{E}})$ can express by

$$SNR(\boldsymbol{\mathcal{R}}, \boldsymbol{\mathcal{E}}) = \frac{\boldsymbol{\mathcal{R}}}{F^2}\sin\left(\sin^{-1}\frac{\boldsymbol{\mathcal{R}}}{\sqrt{\boldsymbol{\mathcal{R}}^2 + \boldsymbol{\mathcal{E}}^2}}\right). \tag{5}$$

Lower $\boldsymbol{\mathcal{E}}$ ensures higher $SNR(\boldsymbol{\mathcal{R}}, \boldsymbol{\mathcal{E}})$ and thus better image quality. Considering Eq (5) based on the minimization addressed by Eq (4), first we will discuss the imaging mode and then optimization in brief.

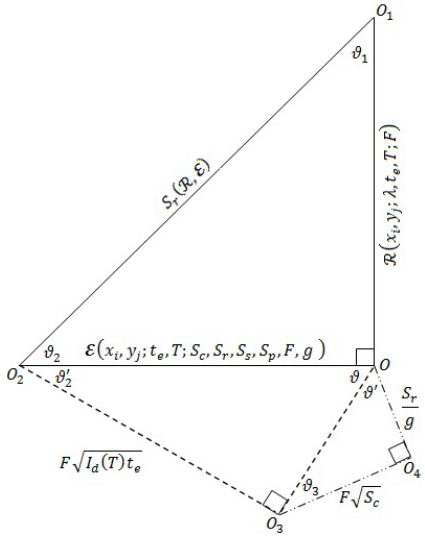

Figure 2. Pythagorean pentagonal expressed based on Eq (3) in case of $S_s\left(x_i, y_j\right) = 0$ and $S_p = 0$. Depend upon the magnitude of involved parameters, the sides of triangles OO_2O_3 and OO_3O_4 change and thus change the length OO_2 of triangle O_1O_2O.

[3]It is an unwanted charges generated in a sensor during the process of charge packets transfer through the sensor's pixel array on account of clocking operation. It reduces the overall image quality.

[4]It is the intrinsic Gaussian noise of the camera, arising during the voltage digitization process of each pixel by an analog-to-digital converter.

[5]It is the ratio of SNR at the input to the SNR at the output of the amplifier stage [*Price et al.*, 1993]. For any given amplifier, the output for a single electron input will vary, typically centered around a mean value. The amplified signal distribution depends on the type of amplifier used, and noise factor ≥ 1.

[6]Referred to as "on-chip multiplication gain", which means multiplication of charge (i.e., electrons) collected in each pixel of the CCD's active array.

A. IMAGING MODE

Depending upon the camera working mode, it can be categorized into two types that are conventional CCD mode and EMCCD mode discussed below. Let $\boldsymbol{\mathcal{E}}_{\mathrm{CCD}}$ and $\boldsymbol{\mathcal{E}}_{\mathrm{EMCCD}}$ are errors in CCD and EMCCD modes respectively. In either mode, we discuss the problem based on a time scale and check absolute errors. Using Eq (5), the SNRs, for instance $SNR_{\mathrm{CCD}}(\boldsymbol{\mathcal{R}}, \boldsymbol{\mathcal{E}})$ and $SNR_{\mathrm{EMCCD}}(\boldsymbol{\mathcal{R}}, \boldsymbol{\mathcal{E}})$ are compared as well.

A.1. CCD Mode

In this mode, CIC noise is negligible, comparable to readout noise, i.e. $S_c \to 0$. Also, the noise factor minimizes, i.e. $F \to 1$. Therefore, the error problem described by Eq (4) simply becomes

$$\boldsymbol{\mathcal{E}}_{\mathrm{CCD}}(t_e; S_r, T) = \lim_{g\to 1} \lim_{F\to 1} \lim_{S_c\to 0} \boldsymbol{\mathcal{E}}(t_e, T; S_c, S_r, F, g)\ . \tag{6}$$

Depending upon the time scale using Eq (6), the error difference under two-time cases can be described by

$$\begin{aligned} \Delta\boldsymbol{\mathcal{E}}_{\mathrm{CCD}} &= (\boldsymbol{\mathcal{E}}_{\mathrm{CCD1}} - \boldsymbol{\mathcal{E}}_{\mathrm{CCD2}}) = \lim_{t_e\to 0} \boldsymbol{\mathcal{E}}_{\mathrm{CCD}}(t_e; S_r, T) - \boldsymbol{\mathcal{E}}_{\mathrm{CCD}}(t_e \gg 0; S_r \ll 1, T) \\ &= S_r - \sqrt{I_d(T) t_e} \end{aligned}\ . \tag{7}$$

The short-time case denoted by $\boldsymbol{\mathcal{E}}_{\mathrm{CCD1}}$ signifies noticeable readout error with negligible dark noise[7] (DN) and vice versa for a long time scale denoted by $\boldsymbol{\mathcal{E}}_{\mathrm{CCD2}}$. Compared to constant $\boldsymbol{\mathcal{E}}_{\mathrm{CCD1}}$, the shot noise $\boldsymbol{\mathcal{R}}_{\mathrm{CCD1}}$ is a linear signal for a short time and $SNR(\boldsymbol{\mathcal{R}}, \boldsymbol{\mathcal{E}}_{\mathrm{CCD1}}) \to 1$. Practically, $SNR(\boldsymbol{\mathcal{R}}, \boldsymbol{\mathcal{E}}_{\mathrm{CCD1}})$ is also time-dependent and increases with time. For a long time both $\boldsymbol{\mathcal{R}}_{\mathrm{CCD2}}$ and $\boldsymbol{\mathcal{E}}_{\mathrm{CCD2}}$ is linear, but$SNR(\boldsymbol{\mathcal{R}}, \boldsymbol{\mathcal{E}}_{\mathrm{CCD2}}) \propto \sqrt{t_e}$.

A.2. EMCCD Mode

In this mode, readout noise is negligible, i.e. $S_r \to 0$. And, the noise factor approaches $\sqrt{2}$, i.e. $F \to \sqrt{2}$ for $g > 1$. The error optimization problem described by Eq (4) becomes

$$\boldsymbol{\mathcal{E}}_{\mathrm{EMCCD}}(t_e; S_c, T) = \lim_{F\to\sqrt{2}} \lim_{S_r\to 0} \boldsymbol{\mathcal{E}}(t_e, T; S_c, S_r, F, g > 1)\ . \tag{8}$$

Depending upon the time scale using Eq (8), the error difference under two-time cases can be described by

$$\begin{aligned} \Delta\boldsymbol{\mathcal{E}}_{\mathrm{EMCCD}} &= (\boldsymbol{\mathcal{E}}_{\mathrm{EMCCD1}} - \boldsymbol{\mathcal{E}}_{\mathrm{EMCCD2}}) = \lim_{t_e\to 0} \boldsymbol{\mathcal{E}}_{\mathrm{EMCCD}}(t_e; S_c, T) - \boldsymbol{\mathcal{E}}_{\mathrm{EMCCD}}(t_e \gg 0; S_c \ll 1, T) \\ &= \sqrt{2}\left[S_c - \sqrt{I_d(T) t_e}\right] \end{aligned}\ . \tag{9}$$

The short-time case denoted by $\boldsymbol{\mathcal{E}}_{\mathrm{EMCCD1}}$ signifies only CIC noise, while the long-time case denoted by $\boldsymbol{\mathcal{E}}_{\mathrm{EMCCD2}}$ holds negligible CIC. Compared to constant $\boldsymbol{\mathcal{E}}_{\mathrm{EMCCD1}}$, the shot noise $\boldsymbol{\mathcal{R}}_{\mathrm{EMCCD1}}$ is a linear signal for a short time and $SNR(\boldsymbol{\mathcal{R}}, \boldsymbol{\mathcal{E}}_{\mathrm{EMCCD1}}) \propto 1/S_c$. Practically, $SNR(\boldsymbol{\mathcal{R}}, \boldsymbol{\mathcal{E}}_{\mathrm{EMCCD1}})$ is also time-dependent and obeys $SNR(\boldsymbol{\mathcal{R}}, \boldsymbol{\mathcal{E}}_{\mathrm{EMCCD1}}) \propto t_e/S_c$. For a long time both $\boldsymbol{\mathcal{R}}_{\mathrm{EMCCD2}}$ and $\boldsymbol{\mathcal{E}}_{\mathrm{EMCCD2}}$ is linear and $SNR(\boldsymbol{\mathcal{R}}, \boldsymbol{\mathcal{E}}_{\mathrm{EMCCD2}}) \propto \sqrt{t_e}$.

B. IMAGING OPTIMISATION

To address the imaging optimization problem dependent on a camera sensor, specifically min. $\boldsymbol{\mathcal{E}}_{\mathrm{Mode}}$, we can adjust the imaging system parameters accordingly. Methods such as binning regulations, tuning time, and adjusting frequency are several ways to achieve this. The optimization process here is detailed in two parts: optimization — 1, which involves spatial feature selection like array size and binning, and optimization — 2, which involves temporal–frequency adjustments. In practice, both optimizations are interconnected through the frame rate per second.

B.1. Optimisation — 1

Pixel binning is a process that allows charge from two or more pixels to be combined on the EMCCD chip before readout. In general, $n \times n$ binning of $H \times V$ active pixels, for $(H, V) \gg n$, means n^2 adjacent pixels are combined to function as a single large pixel. For instance, 1×1 binning means each $H \times V$ pixel of size $W \times H$ μm is individually used, while 2×2 binning means 4 adjacent pixels are combined to act as one. Instead of squared array size regime pixel binning (shown blue shaded in Table 3), a non-squared regime (orange shaded) is also an option.

[7]It is a noise that persists even when there is no light present, caused by thermal energy pushing electrons from the valence band to the conduction band, resulting in spontaneously generated electrons.

Table 3 Imaging frame rates on binning pattern and array size. Comparing ratios array size over binning, for instance $\frac{128\times128}{1\times1} \approx \frac{256\times256}{2\times2} \approx \frac{512\times512}{4\times4} \rightarrow 210$, $\frac{64\times64}{1\times1} \approx \frac{128\times128}{2\times2} \approx \frac{256\times256}{4\times4} \rightarrow 390$, etc. frame rate is nearly the same[8].

Binning	**Array Size**						
	512×512	256×256	128×128	64×64	512×100	512×32	512×1
1×1	56	110	212	398	267	708	2881
2×2	109	210	394	699	486	1141	–
4×4	206	385	682	1109	820	1615	–

Summing the charge from multiple pixels provides better noise performance than reading out each pixel individually. This optimization therefore can be named as the binning regulation. Practically, it follows two steps: vertical binning and then horizontal.

- Vertical binning. Charge from two or more rows on the EMCCD chip is moved down into the shift register before readout. The number of rows shifted depends on the chosen binning pattern.
- Horizontal binning. Charge from two or more pixels in the serial register is transferred into the output amplifier and read out as a single combined data value.

Selecting the appropriate $n \times n$ binning pattern is crucial so that photon detection from an ion on a binning area is not superimposed by photons of other neighboring ions of the trap volume. Pixel binning effectively increases the pixel size resulting in increased sensitivity [*Zhang et al.*, 2010].

B.2. Optimisation — 2

Imaging of trapped ions in the given t_e valued both $\boldsymbol{\mathcal{R}}$ and $\boldsymbol{\mathcal{E}}$, which consequently determines resolution. Concerning t_e, there are several other time intervals, mentioned below, that can tune resolution.

- Read time (t_h). Time required for the serial conversion per pixel. For both modes, the horizontal readout rate (MHz) expressed by $f_h = 1/t_h$ at 16 −bit are as follows.
  - CCD mode. In the case of conventional amplifying mode, f_h as $f_{\mathrm{CCD}-h}$ available for selection are $f_{\mathrm{CCD}-h} = 0.08{,}1$ and 3.
  - EMCCD mode. In the case of EMCCD amplifying mode, f_h as $f_{\mathrm{EMCCD}-h}$ available for selection are $f_{\mathrm{EMCCD}-h} = 1{,}5{,}10$, and 17 with 17 MHz at 26 fps (frame per second).

  Concerning f_h related to S_r, it has already been reported that S_r increases with f_h such that $S_{r,\mathrm{EMCCD}-h} \approx 65\mathrm{e}^-$ RMS at 10 MHz, which can reduced to $< 1\mathrm{e}^-$ by applying $g \approx 65$. $S_{r,\mathrm{CCD}-h}$ and $S_{r,\mathrm{EMCCD}-h}$ are read noise in CCD and EMCCD modes respectively. Depend upon f_h selected, the frame rate let's denote by f_{ps} can also be determined accordingly.
  - f_h low means slower readout cause S_r low and f_{ps} low but dynamic range higher.
  - f_h high means higher readout cause S_r increases and f_{ps} high but dynamic reduced.

  So notationally, $f_h \propto (S_r, f_{ps})$ can be stated as one of the articulations. Based on f_h, the error optimization that is $\boldsymbol{\mathcal{E}} \rightarrow \boldsymbol{\mathcal{E}}_{min.}$ can be checked in both modes separately. For CCD mode by selecting $f_{\mathrm{CCD}-h}$ low, while for EMCCD mode: (1) at a low rate by selecting $f_{\mathrm{EMCCD}-h}$ low and (2) at a high rate by selecting $f_{\mathrm{EMCCD}-h}$ high with $g \gg 1$.
- Row shift time (t_v). The time required for a parallel shift of row charges vertically is also known as vertical shift time. t_v is user-selectable mentioned in Table 2. Depend upon t_v, $\boldsymbol{\mathcal{E}}$ can be tuned.
  - t_v low means a faster vertical speed cause S_c low (without image distortion) and vertical smearing[9] (VS) reduced for t_e low. The charge transfer efficiency[10] (CTC) and pixel well depth[11] (PWD) also reduce, which is crucial for bright sources, as pixel with large signal is more prone to retaining some charge, thereby degrading spatial resolution.
  - t_v high means a slower vertical clock cause S_c high and vertical smearing also reduces during low t_e. CTC gets better, and PWD increases but f_{ps} low.

  So notationally, in a rough manner $t_v \propto (S_c,$ VS, CTC, PWD, $1/f_{ps})$ can be stated as another articulation. To improve CTC, the vertical clocking voltage, let's V_v, can be increased using vertical

[8]Manual, version 2.1 rev 26 Sept 2023 (https://andor.oxinst.com/downloads/uploads/ixon-ultra-hardware-user-guide.pdf).

[9]Vertical smearing occurs when light falls on the image area during short time required transferring charge from the image area to the storage area. If exposure time is comparable to this transfer time, pixels shifting vertically through brighter regions of the image collect "extra" charge, resulting in vertical streaking.

[10]The fraction of electrons that are sucessfully moved from one to another during read-out.

[11]PWD is the charge amount a pixel can hold before saturation. The active area PWD is 180,000 e^-, while the gain register PWD is 800,000 e^- for 512×512 active pixels.

clock voltage amplitude. V_v high cause CTC low but S_c high. Notationally, $V_v \propto (1/\text{CTC}, S_c)$ can be another articulation. For short exposures, e.g. $t_e = 1\text{ms}$, with a high signal count and DC illumination, it is necessary for V_v to increase to ensure that the keep clean cycle[12] (KCC) can fully remove the extremely high (saturated) signal that may have accumulated during the sensor readout phase.

- Shutter open time (t_o) and shutter close time (t_c). That is delay times. Under normal operation, the shutter should be set to permanently open so that $(t_o, t_c) \to 0$.

Relating f_h, t_v and V_v with the temperature regulation of the camera, heat generation (HG) is primarily from the vertical clocks while the increase in $f_h$has negligible impact. Increase in V_v also results the heat generation.

Tuning various time and frequency variables to minimize error signals is crucial and depends on the specific nature of the experiment. This optimization therefore can be named as the time–frequency regulation. Summarizing all such time variables while balancing the corresponding noise in an experiment is quite complex. For simplicity and clarity, Fig 3 presented provides a pictorial representation of the relationship between noise and time variables. This visual aid helps in easily determining the necessary compromises regarding the noise in an experiment. The above articulations are used for this time–frequency-based noise mapping. While these conclusions are specific to the Andor iXon U897, similar articulations can be made for other camera models as well.

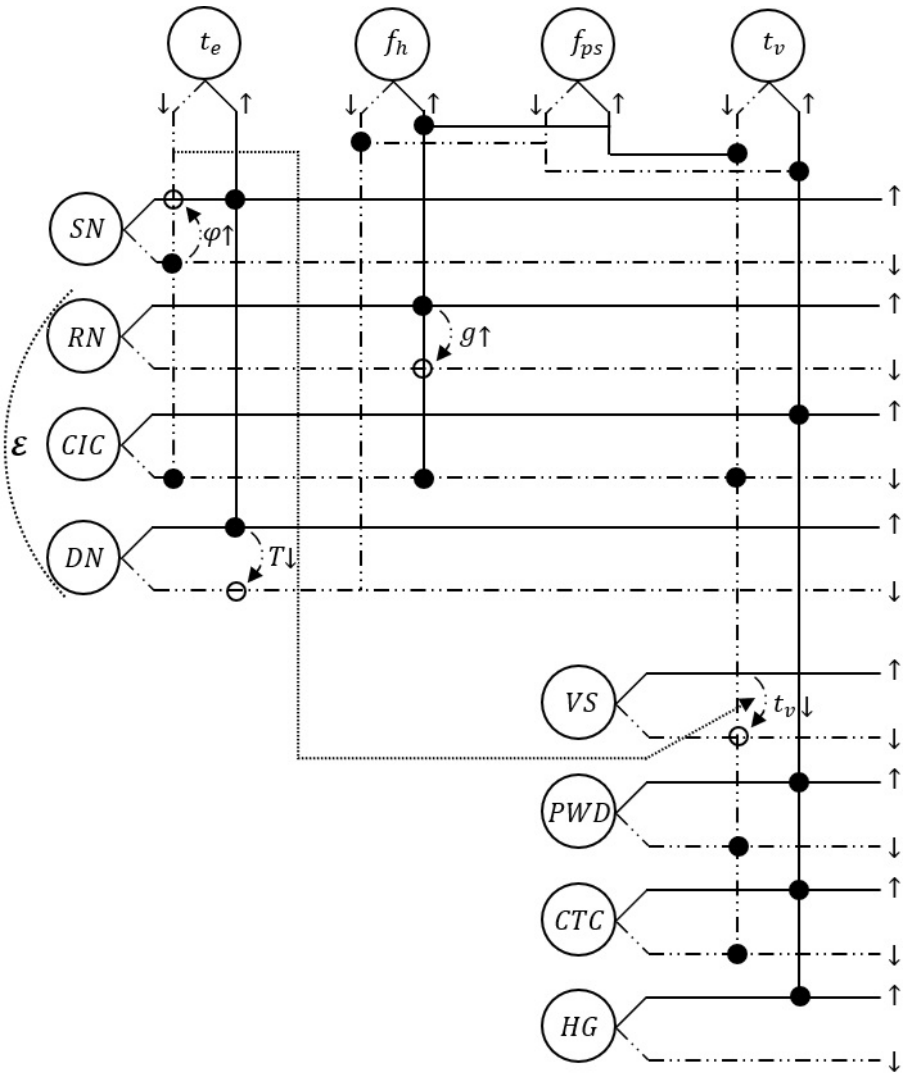

Figure 3. Time–frequency-based noise mapping to $\min.\boldsymbol{\mathcal{E}}_{\text{Mode}}$ for both CCD and EMCCD modes, based on Eq (3), to $\max.SNR_{\text{Mode}}(\boldsymbol{\mathcal{R}}, \boldsymbol{\mathcal{E}})$. Arrows ↑(↓) indicate low(high) values of the parameters, while ● indicates the dependency of parameters, for instance t_e in both low(high) cases influences CIC and DN but is independent of RN. ○ indicates switching under condition, for instance f_h(high) cause RN(high) can be switched to RN(low) by increasing g. φ is the mean incident photon flux described by $\mathcal{U}(x_i, y_j)/t_e$.

[12]Both the image and storage areas of the EMCCD must be thoroughly cleaned out, such a process known as KCC. This continuous cleaning ensures the camera is always ready to start an acquisition when needed.

Conclusions

The developed imaging setup for the electron–ion trapping experiment has been reported. This simple and cost-effective setup features a multi-lens system positioned outside the vacuum chamber, offering a numerical aperture of 0.375, a magnification greater than 10x, and a resolution of up to 1 μm is reasonable. This adheres to the primary design principle of the imaging optical setup. However, while maintaining the same optical array structure, there remains the potential for adjusting the system's magnification and increasing the fraction of the solid angle in the future as needed. Currently, spherical aberration has not been addressed, which constitutes the second design principle, and can be managed later as necessary. Improving the signal-to-noise ratio, the third principle is being investigated by identifying various noise sources and optimizing operational parameters to suppress them.

Acknowledgments. We acknowledged funding from the Czech Science Foundation (GAČR: GA24-10992S), from the Primus Research Programme (PRIMUS/21/SCI/005), and from the Charles University Grant Agency (GAUK 295023, GAUK 131224). We also acknowledge the support from the Czech Ministry of Education, Youth and Sports (project QM4ST, reg. no. CZ.02.01.01/00/22_008/0004572) and from the Faculty of Mathematics and Physics of Charles University.

References

Alberti, Andrea, et al. Super-resolution microscopy of single atoms in optical lattices. *New Journal of Physics* 18.5 (2016): 053010.

Alt, Wolfgang. An objective lens for efficient fluorescence detection of single atoms. *Optik* 113.3 (2002): 142–144.

Blatt, Rainer, et al. Quantum simulations with trapped ions. *Nature Physics* 8.4 (2012): 277–284.

Daigle, Olivier, et al. Time-delay integration EMCCD. *2019 Photonics North (PN)*. IEEE, 2019.

Eva, Rittweger. STED microscopy reveals crystal colour centres. *Nature Photon* 3 (2009): 144–147.

Kumar, Vineet, et al: Mechanics of the Dual-Frequency Paul Trap, 32nd Annual Student Conference, *Week of Doctoral Students* 2023, 178–184

Leibfried, D., et al. Experiments towards quantum information with trapped Calcium ions. *AIP Conference Proceedings*. Vol. 551. No. 1. American Institute of Physics, 2001.

Noek, Rachel, et al. High speed, high fidelity detection of an atomic hyperfine qubit. *Optics letters* 38.22 (2013): 4735–4738.

Nordmann, T., et al. Bichromatic UV detection system for atomically-resolved imaging of ions. *Review of Scientific Instruments* 94.6 (2023).

Price, John, et al. Signals and noise. *Telecommunications Engineer's Reference Book*. Butterworth-Heinemann, 1993. 10-1.

Schiffer, J. P., et al. Temperature, ordering, and equilibrium with time-dependent confining forces. *Proceedings of the National Academy of Sciences* 97.20 (2000): 10697–10700.

Wong-Campos, J. D., et al. High-resolution adaptive imaging of a single atom. *Nature Photonics* 10.9 (2016): 606–610.

Zhang, Wen W., et al. Signal-to-Noise Ratio Improvement of EMCCD Cameras. *World Academy of Science, Engineering and Technology* 4.5 (2010): 966–970.

Appendix — 1

The parameters y_j, mentioned in Eq (1), are given below by Eq (A1.1), which are functions of variables x_j. For the purpose of evaluation of our setup, the cascaded arrangement of matrix multiplication so taken is $M_I = D_8L_4D_7M_2D_6M_1D_5L_3D_4D_3L_2D_2'D_2L_1D_1$, where D_j's are the distance matrices, L_j's are the lens matrices and M_j's are the unit plane mirror matrices.

$$\left.\begin{aligned} y_1 &= x_1\left(1+\tfrac{t_2}{r_2}\tfrac{1-n}{n}\right)+\left(x_2+x_1(d_3+d_4)\right)\tfrac{1-n}{r_2} \\ y_2 &= x_1\left(d_3+d_4+\tfrac{t_2}{n}\right)+x_2+d_2\left\{x_1\left(1+\tfrac{t_2}{r_2}\tfrac{1-n}{n}\right)+\left(x_2+x_1(d_3+d_4)\right)\tfrac{1-n}{r_2}\right\} \\ y_3 &= x_3\left(1+\tfrac{t_2}{r_2}\tfrac{1-n}{n}\right)+\left(x_4+x_3(d_3+d_4)\right)\tfrac{1-n}{r_2} \\ y_4 &= x_3\left(d_3+d_4+\tfrac{t_2}{n}\right)+x_4+d_2\left\{x_3\left(1+\tfrac{t_2}{r_2}\tfrac{1-n}{n}\right)+\left(x_4+x_3(d_3+d_4)\right)\tfrac{1-n}{r_2}\right\} \end{aligned}\right] \quad \text{(A1.1)}$$

The parameters x_j depending upon the spacing variables are given by Eq (A1.2) with constants $C_1 = \frac{1-n}{r_4} + \frac{t_4}{{r_4}^2}\frac{(1-n)^2}{n}$ and $C_2 = 1+\frac{t_4}{r_4}\frac{1-n}{n}$, which are optics parameter dependent.

$$\left.\begin{aligned} x_1 &= C_1 d_8 + C_2 + \frac{1-n}{r_3}\left\{\frac{t_4}{n} + C_2 d_8 + (C_1 d_8 + C_2)(d_5 + d_6 + d_7)\right\} \\ x_2 &= (C_1 d_8 + C_2)\frac{t_3}{n} + \left(1 + \frac{t_3}{r_3}\frac{1-n}{n}\right)\left(\frac{t_4}{n} + C_2 d_8 + (C_1 d_8 + C_2)(d_5 + d_6 + d_7)\right) \\ x_3 &= C_1 + \frac{1-n}{r_3}(C_1(d_5 + d_6 + d_7) + C_2) \\ x_4 &= C_1\frac{t_3}{n} + \left(1 + \frac{t_3}{r_3}\frac{1-n}{n}\right)(C_1(d_5 + d_6 + d_7) + C_2) \end{aligned}\right] \quad \text{(A1.2)}$$

Appendix — 2

Concerning the diffraction-limited spot size[13] (d_{Airy}) and pixel size (d_{pixel}), for an optical imaging system, the imaging of atomic samples in two cases: ^{40}Ca imaging and $^{40}Ca^{+}$ imaging are discussed as follows. Using the Rayleigh criterion, $d_{\text{Airy}} = 1.22\lambda/NA$, the image size of the diffraction-limited spot (Airy disk) can be expressed by $d_{\text{I\_Airy}} = M \times d_{\text{Airy}}$, so that image sampling ($s_{\text{I\_Airy\_sam}}$) is given by $s_{\text{I\_Airy\_sam}} = d_{\text{I\_Airy}}/d_{\text{pixel}}$. M is the magnification. If $s_{\text{I\_Airy\_sam}} < 2$ then the system is said to be under-sampling as the details about d_{Airy} limiting resolution on the account of $d_{\text{I\_Airy}}$ is compromised. Similarly, the spatial resolution (or the effective spatial resolution[14]) of the imaging system depends upon d_{pixel} and M can be expressed by $d_{\text{res}} = d_{\text{pixel}}/M$, which means the separation between two particles (d_{sep}) must possess the condition $d_{\text{sep}} \geq d_{\text{res}}$ for particles to be distinguished as distinct objects.

Considering the atom size d_{atom}, a comparative analysis involving d_{Airy}, d_{pixel} and d_{sep} leads to the following understanding.

- ^{40}Ca **Imaging**. Practically $d_{\text{atom}} \ll (d_{\text{Airy}}, d_{\text{pixel}})$, which means the individual ^{40}Ca atom of cloud, cannot be resolved. However, since the goal is to image the fluorescence of a beam, therefore we are not concerned with resolving individual atoms, but with imaging the macroscopic distribution of light emitted by many calcium atoms. For fluorescence of width **(d_{flu})**, the image width on the detector is $d_{\text{I\_flu}} = M \times d_{\text{flu}}$ so that the image sampling is $s_{\text{I\_flu\_sam}} = d_{\text{I\_flu}}/d_{\text{pixel}}$, which represents the number of pixels covered by the fluorescence signal.
  - If $d_{\text{flu}} < d_{\text{res}}$ means $s_{\text{I\_flu\_sam}} < 1$ then the image will be blurred.
  - If $d_{\text{flu}} > xd_{\text{res}}$ means $s_{\text{I\_flu\_sam}} > x$ for $x > 3$ (means the image is sampled across many pixels) then the macroscopic details of the signal can be captured. Any spatial variations within the signal that are smaller than d_{Airy} will be blurred or averaged out.
- $^{40}Ca^{+}$ **Imaging**. Since the size of an ion $d_{\text{ion}} \ll (d_{\text{Airy}}, d_{\text{pixel}})$, where $d_{\text{ion}} \cong d_{\text{atom}}$, individual $^{40}Ca^{+}$ ions within the ionic cloud cannot be properly resolved. Instead, the entire cloud ($d_{\text{ion\_cloud}}$) appears as a larger spot such that each $^{40}Ca^{+}$ ion's contribution to the image is blurred. $^{40}Ca^{+}$ ions are too small to be resolved, but the overall cloud can still be imaged as long as $d_{\text{ion\_cloud}} > d_{\text{Airy}}$, where the cloud scale[15] as $d_{\text{ion\_cloud}} \propto n_{\text{ion}}^{1/3}$, with n_{ion} representing the number of ions. Thus, the inequality $n_{\text{ion}}^{1/3} > \frac{d_{\text{Airy}}}{D_{\text{cri-den}}}$ can be used, depending on the ion density, where $D_{\text{cri\_den}} = (6/\pi\rho)^{1/3}$ is the critical distance for a given cloud density.

  Depending upon n_{ion} and the average separation between ions $d_{\text{ion\_sep}} = d_{\text{sep}}$, the imaging dynamics on account of a condition $d_{\text{ion\_cloud}} \gg d_{\text{pixel}}$ (or $n_{\text{ion}}^{1/3} \gg \frac{d_{\text{pixel}}}{D_{\text{cri-den}}}$) addresses the following.
  - If $d_{\text{ion\_sep}} > d_{\text{pixel}}$ then individual $^{40}Ca^{+}$ ions can be able to be distinguished.
  - If $d_{\text{ion\_sep}} < d_{\text{pixel}}$ (i.e. dense crystal), then the system will not be able to resolve individual $^{40}Ca^{+}$ ions, and therefore will appear as a blurred collective.

  Based on these two inequalities, an imaging dynamic function can be formulated at this stage, incorporating $d_{\text{ion\_sep}}$, which is determined by the equilibrium between the Coulomb force (F_{Coul}) and the restoring force (F_{trap}) acting on a particle localized within the crystal. In a trapping field, ions exhibit two distinct types of motion: fast oscillatory motion (micromotion) and slower oscillatory motion (secular motion). It has been reported that the secular motion is much larger (up to seven orders

[13]It is the smallest area that light can be focused, **it**s a theoretical limit, due to the wave nature of light. This means features smaller than d_{Airy} will blur.

[14]Taking in to account d_{pixel}, it defines how much the image is magnified before it is projected onto the detector. This means two points must be separated by d_{pixel} to be distinguished as distinct objects.

[15]For a spherical Coulomb crystal with a uniform density ρ, the total number of ions can be expressed as $n_{\text{ion}} = \rho V$, where the volume V of the ion cloud is given by $V = \frac{4\pi}{3}\left(d_{\text{ion\_cloud}}/2\right)^3$.

of magnitude larger) than the fast oscillatory motion in terms of displacement, particularly at low temperatures where ions are cooled [*Schiffer et al.,* 2000].

The secular motion is the slow, periodic motion of ions within the pseudo-potential created by the time-averaged effect of the rapidly oscillating RF fields, reflecting the long-term behavior of ions in the trap. The restoring force is related with the secular frequency, which governs the secular motion of ions in the trap. In essence, secular motion represents the impact of the restoring force exerted by the trap field, while secular frequency describes the rate of this slow oscillatory motion. Concerning the secular frequency as reason of $d_{\text{ion\_sep}}$ in cloud[16], in simplicity, a dynamic function for our two-frequency Paul trap [*Kumar et al.,* 2024] can be expressed by

$$f\left(n, q_{xj}; D_{\text{cri\_fre}}, d_{\text{pixel}}\right) = D_{\text{cri\_fre}} \sqrt[-\frac{1}{3}]{\frac{q_{x0}}{n^2} + \frac{q_{x1}^2}{2}\left(1 + \frac{1}{n^2}\frac{q_{x2}^2}{q_{x1}^2}\right)} - d_{\text{pixel}} \,. \tag{A2.1}$$

$D_{\text{cri\_fre}} = (e^2/\pi\,\epsilon_o m\omega_1^2)^{1/3}$ is the critical distance for a given cloud one-frequency. Depending upon the parameters selected, one can assess particle distinguishability.

[16]In equilibrium, where $F_{\text{Coul}} = F_{\text{trap}}$, the ion spacing is given by $d_{\text{ion\_spa}} = (e^2/4\pi\epsilon_0 m\omega^2)^{1/3}$, where $e(m)$ is the charge(mass) of an ion and ϵ_0 is the permittivity of free space. ω is the frequency of oscillation.